Computers and Geotechnics 53 (2013) 60–67

Contents lists available at SciVerse ScienceDirect

Computers and Geotechnics

journal homepage: www.elsevier.com/locate/compgeo

Quantitative risk assessment of landslide by limit analysis and random fields

J. Huang [a,*], A.V. Lyamin [a], D.V. Griffiths [a,b], K. Krabbenhoft [a], S.W. Sloan [a]

[a] ARC Centre of Excellence for Geotechnical Science and Engineering, The University of Newcastle, NSW, Australia
[b] Colorado School of Mines, Golden, Colorado, USA

ARTICLE INFO

Article history:
Received 1 March 2013
Received in revised form 16 April 2013
Accepted 21 April 2013
Available online 1 June 2013

Keywords:
Landslide
Risk assessment
Limit analysis
Random field

ABSTRACT

Risk may be estimated by multiplying the probability of failure by the consequence. This is acceptable for systems that have a single mode of failure. For systems that have multiple failure modes, such as landslides, the consequences should be assessed individually for each of the failure modes. This paper proposes a new framework of quantitative landslide risk assessment, in which consequences are assessed individually. The framework is generally applicable, and the landslide risk assessments of two typical slopes are presented.

1. Introduction

The evaluation of the stability of natural or constructed slopes has traditionally been based on a deterministic approach and quantified by a safety factor. In such an approach, geotechnical engineers try to deal with uncertainties by choosing reasonably conservative parameters. However, it is common to use the same safety factor for different type of application without regard to the degree of uncertainty involved in its calculation. Through regulation or tradition, the same safety factor is often applied to conditions that involve widely varying degrees of uncertainty. Since this is not a very logical strategy [4], numerous studies have been undertaken in recent years to develop probabilistic methods that deal with uncertainties in a systematic way (e.g., [14,8,5,9,2,10, 11,22]). Of particular importance has been the development of the random finite element (RFEM) to model the spatial variability of soil properties (e.g., [9]). It is noted, however, that all numerical studies are aimed at pursuing more rigorous methods of estimating the probability of failure (p_f). The overall risk is then calculated as

$$R = p_f \times C \tag{1}$$

where R is the risk and C is the consequence.

The above method works well for systems that have a single failure mode. In landslide problems, as noted by Chowdhury and Xu [3] and Huang et al. [11], multiple failure modes coexist. Because failure modes and consequences are correlated, the consequence associated with each failure mode should be assessed individually, leading to a modified definition of risk as

$$R = \sum_{i=1}^{n_f} p_{fi} \times C_i \tag{2}$$

where p_{fi} and C_i are the probability and consequence of failure mode i, and n_f is the number of identifiable failures.

To be able to use Eq. (2), one needs to assess p_{fi} and C_i individually for each failure. This can be achieved easily in the framework of Monte Carlo simulation. Using this framework, the new method (i.e., Eq. (2)) and the traditional method (i.e., Eq. (1)) are contrasted in Fig. 1, where N_{sim} is the number of simulations.

The new framework has two key modules, i.e., a module to assess safety and a module to assess consequence. In this study, the limit analysis programs developed at the University of Newcastle [18–20,15,16,13] are adopted to check the safety. Both lower bound and upper bound analyses are carried out, and a brief review of the methods will be given in the next section. Because the volume of the sliding mass is directly related to the consequence of a landslide, this quantity is used to quantify consequence in this study. A more complete assessment of the consequence should also quantify the dynamic behaviour of the sliding soil, which will be explored in a future paper. To identify the volume of the sliding soil used to be thought of as a difficult task, but this study shows that the classic K-means clustering method (e.g., [1]) works very well for this purpose. A brief review of this method is presented

* Corresponding author. Tel.: +61 2 49215118.
E-mail address: jinsong.huang@newcastle.edu.au (J. Huang).

0266-352X/$ - see front matter © 2013 Elsevier Ltd. All rights reserved.
http://dx.doi.org/10.1016/j.compgeo.2013.04.009

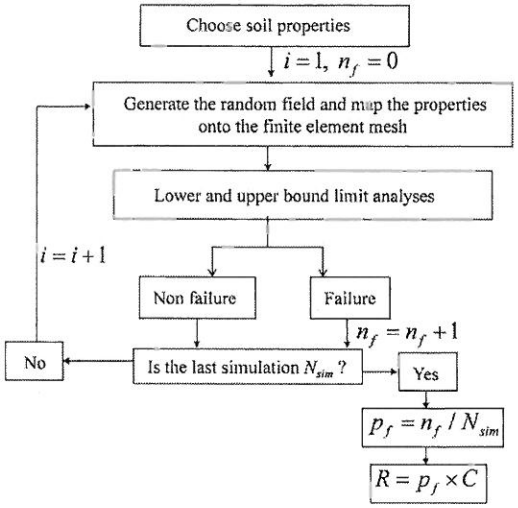

(a) Traditional risk assessment

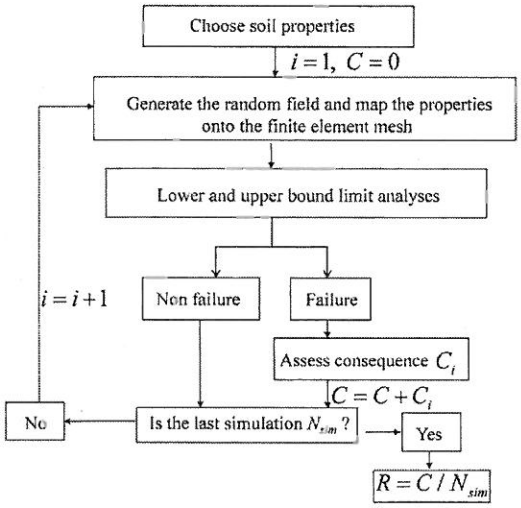

(b) New quantitative risk assessment

Fig. 1. Traditional and new frameworks of risk assessment.

in Section 3. When spatial variability needs to be taken into account, which is especially the case in landslide risk assessment, a third module to generate random fields is needed. While there are several options available for achieving this goal (e.g., [6]), we have chosen the Karhunen–Loeve expansion method to be used in tandem with our limit analysis programs. A brief review of the Karhunen–Loeve expansion method is given in Section 4. Two examples are given in Section 5 to illustrate the new framework. Both examples show that the proposed framework is necessary for a quantitative assessment of landslide risk.

2. Review of finite element limit analysis

The lower and upper bound theorem of classical plasticity theory is a powerful tool for analyzing the stability of problems in soil mechanics. The theory assumes a perfectly plastic soil model with an associated flow rule. The lower bound theorem states that any statically admissible stress field will furnish a lower bound (or 'safe') estimate of the true limit load. A statically admissible stress field is one which satisfies (a) the stress boundary conditions, (b) equilibrium, and (c) the yield condition (the stresses must lie inside or on the yield surface in stress space).

The upper bound theorem states that the load (or the load multiplier), determined by equating the internal power dissipation to the power expended by the external loads in a kinematically admissible velocity field, is not less than the actual collapse load. Based on the duality between the upper and lower bound methods, Krabbenhoft et al. [13] derived an upper bound formulation in terms of stresses rather than velocities and plastic multipliers. This allows for a uniform implementation of lower and upper bound theorem in the mathematical programming form as

$$\begin{aligned} &\text{maximize} && \alpha \\ &\text{subject to} && \mathbf{A}\sigma = \alpha\mathbf{p} + \mathbf{p}_0 \\ &&& \mathbf{f}(\sigma) \leqslant 0 \end{aligned} \tag{3}$$

where $\mathbf{A}$ is an equilibrium matrix (which also contains boundary conditions), $\boldsymbol{\sigma}$ is a vector of stresses, the external load consists of a constant part $\mathbf{p}_0$ and a part proportional to a scalar parameter α, and $\mathbf{f}$ defines the yield condition.

It should be mentioned that the matrix $\mathbf{A}$ in Eq. (3) can be amended to include stress or velocity discontinuities, which have previously been shown to be very efficient (e.g., [20]).

Although Eq. (3) can be solved by public-domain second order cone programming packages (e.g., SeDumi and Mosek), our in-house solvers and limit analysis programs are used in this study [15,16,13].

3. The *K*-means clustering method

Although static analyses are conducted in this study, the nodal displacements at the limit state are still useful indicators of a landslide. It is, however, unsatisfactory to use any predefined threshold of displacement to identify the sliding mass and, from the point of view of classification, a sliding mass can be identified without using such a threshold. Although there many sophisticated classification techniques are available (e.g., [1]), the classic *K*-means algorithm works perfectly well for the application considered in this study. Consider a set of observations $(\mathbf{d}_1, \mathbf{d}_2, \ldots, \mathbf{d}_N)$, where each observation is an m-dimensional real vector, the *K*-means method aims to cluster the N observations into K sets ($K \leqslant N$) by minimizing a squared error function of the form

$$J = \sum_{k=1}^{K}\sum_{n=1}^{N}\left\|\mathbf{d}_n^{(k)} - \mathbf{c}_k\right\|^2 \tag{4}$$

where $\mathbf{c}_k (k = 1, \ldots K)$ is the cluster centre.

Given $\mathbf{c}_k^i$ at iteration i, the *K*-means clustering method computes $\mathbf{c}_k^{i+1}$ by the following two steps:

(a) *Assign set k to observation* $\mathbf{d}_n$ *by minimizing the squared error function J.*
(b) *Update cluster centres* $\mathbf{c}_k^{i+1}$ *by means of* $\mathbf{d}_n^{(k)}$.

Stop when $\mathbf{c}_k^{i+1} = \mathbf{c}_k^i$. For the first iteration, $\mathbf{c}_k^0$ can be set randomly.

In this study, the nodal displacements serve as observations $(\mathbf{d}_1, \mathbf{d}_2, \ldots, \mathbf{d}_N)$, where N is the number of nodes. The number of sets (K) is two (i.e., stable and sliding masses).

4. The Karhunen–Loeve expansion method

There are several random field generation methods available (see, for example, [6]). The Karhunen–Loeve expansion method was chosen because it has analytical solutions for the exponential covariance function considered in this study.

Let $X(\mathbf{x}, \omega)$ be a random field, where $\mathbf{x} \in D$ (physical space) and $\omega \in \Omega$ (a probability space). The covariance function, denoted as $C_X(\mathbf{s}, \mathbf{t})$, where $\mathbf{s}, \mathbf{t} \in D$, is bounded, symmetric and positively defined. Using Mercer's Theorem, it can be decomposed according to

$$C_X(\mathbf{s}, \mathbf{t}) = \sum_{i=1}^{\infty} \lambda_i f_i(\mathbf{s}) f_i(\mathbf{t}) \tag{5}$$

where λ_i and $f_i(\mathbf{x})$ are the eigenvalues and eigenfunctions of $C_X(\mathbf{s}, \mathbf{t})$, respectively.

The eigenfunctions $C_X(\mathbf{s}, \mathbf{t})$ form a complete orthogonal set satisfying

$$\int_D f_i(\mathbf{s}) f_i(\mathbf{t}) d\mathbf{x} = \delta_{ij} \tag{6}$$

Based on Eq. (6), the eigenvalues and eigenfunctions of $C_X(\mathbf{s}, \mathbf{t})$ are the solutions of the following Fredholm equation:

$$\int_D C_X(\mathbf{s}, \mathbf{t}) f(\mathbf{s}) = \lambda f(\mathbf{t}) \tag{7}$$

Numerical methods are usually required to solve Eq. (7), although exact solutions are available for some classes of covariance function (see, for example, [12,17]). Zhang and Lu [21] presented an analytical solution for an exponential covariance function. The computation involves only the solution of a one-dimensional super characteristic equation (i.e., (11)).

The exponential covariance function in one dimension is

$$C_X(x_1, x_2) = \sigma_X^2 \exp\left(\frac{-|x_1 - x_2|}{\theta_x}\right) \tag{8}$$

where σ_X is the standard deviation and θ_x is the spatial correlation length. θ_x is also called the scale of fluctuation, which is equal to twice the so-called autocorrelation distance.

The eigenvalues and their corresponding eigenfunctions can be expressed as

$$\lambda_i = \frac{2\theta_x \sigma_X^2}{\theta_x^2 w_i^2 + 1} \tag{9}$$

$$f_i(x) = \frac{1}{\sqrt{\frac{1}{2}(\theta_x^2 w_i^2 + 1) + \theta_x}} [\theta_x w_i \cos(w_i x) + \sin(w_i x)] \tag{10}$$

where w_n are positive roots of the characteristic equation:

$$\theta_x(\theta_x^2 w^2 - 1)\sin(wL) = 2\theta_x w \cos(wL) \tag{11}$$

and L is the length of the random field.

For two-dimensional problems, Eq. (8) can be written as

$$C_X((x_1, y_1), (x_2, y_2)) = \sigma_X^2 \exp\left(\frac{-|x_1 - x_2|}{\theta_x}\right) \exp\left(\frac{-|y_1 - y_2|}{\theta_y}\right) \tag{12}$$

and Eq. (7) can be solved independently for each dimension yielding the eigenvalues and eigenfunctions as

$$\lambda_{i,j} = \lambda_i^{(x)} \lambda_j^{(y)} \tag{13}$$

$$f_{i,j}(x, y) = f_i(x) f_j(y) \tag{14}$$

Since Eq. (5) has to be truncated to a finite number of terms, a significant concern is that the simulated variance will be reduced. In order to control this reduction, the eigenvalues are sorted in descending order and the number of terms is decided when the eigenvalues have decayed enough to satisfy the condition

$$\frac{\lambda_n}{\lambda_1} \leqslant \text{Tol} \tag{15}$$

where Tol is typically set to 10^{-5}. Figs. 2 and 3 show how the eigenvalues decay in one and two dimensions, where Θ is the dimensionless spatial correlation length defined as

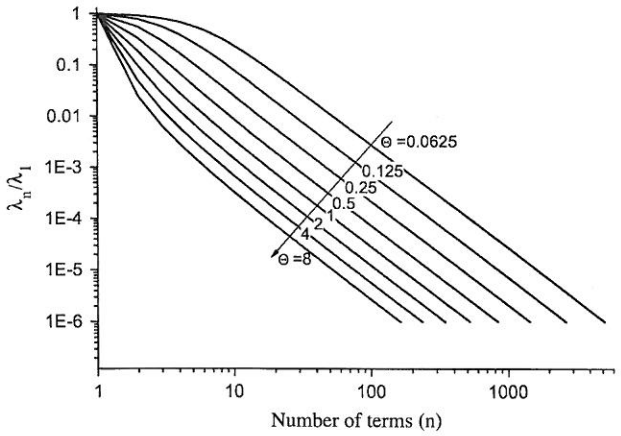

Fig. 2. Decay of eigenvalues in one dimension.

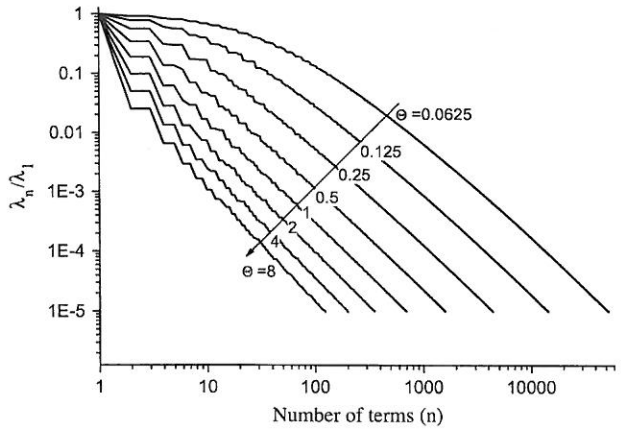

Fig. 3. Decay of eigenvalues in two dimensions.

$$\Theta = \frac{\theta}{L} \tag{16}$$

It can be seen from these figures that the required number of terms increases when the spatial correlation length decreases. For the smallest Θ considered in this study, more than 50,000 terms are used.

5. Examples

The landslide risks of two hypothetical slopes are assessed in this section. Both slopes are assumed to fail under undrained conditions, with the undrained shear strength being modelled as a random field. The Tresca failure criterion is used in the limit analysis calculations and all other parameters are assumed to be deterministic. Two thousand Monte Carlo simulations were carried out for the cases where p_f is larger than 10%. More simulations were conducted for other cases to ensure that the maximum error in p_f is less than 0.01 at a confidence level of 90%. The first example is a slope in a uniform layer. The histogram of the sliding mass at collapse suggests a wide range of consequences, which implies that the proposed framework should be adopted. Parametric studies, carried out to investigate the influence of anisotropic random fields on the risk of a landslide, suggest that the horizontal spatial correlation length has a much more significant effect on the risk than the vertical spatial correlation length. The second example is for a slope in a two layered soil, with the undrained shear strengths

being modelled by two independent random fields. The coexistence of two (i.e., shallow and deep) failure mechanisms is shown clearly by the histograms of the sliding mass at collapse. Both examples show that the proposed risk assessment framework must be used to obtain a quantitative estimate of the risk.

5.1. Undrained slope failure in a uniform layer

The profile of the slope in a uniform layer is shown in Fig. 4. The slope has a height $H = 10$ m and soil has a unit weight of $\gamma_1 = 20$ kN/m^3 and an undrained shear strength of $c_u = 50$ kPa. The boundary conditions are rollers on the left and right vertical boundaries, and full fixity at the base. Deterministic limit analyses indicate that the lower and upper bounds on the safety factor are 1.446 and 1.494, respectively. The safety factor obtained by an elasto-plasticity finite element analysis based on strength reduction method is 1.465.

Probabilistic analyses are carried out according to the proposed framework (Fig. 1b). The undrained shear strength is assumed to be a lognormally distributed random variable with mean $\mu_{c_u} = 50$ kPa and a coefficient of variation $V_{c_u} = 0.5$. In the following, the dimensionless spatial correlation length is defined as

$$\Theta = \frac{\theta}{H} \tag{17}$$

Note that this definition is different from Eq. (16), where the maximum side length of the random field is used.

Fig. 5 shows the histogram of the sliding mass at collapse from 2000 lower bound simulations for the case $\Theta_x = 2$ and $\Theta_y = 0.25$. In this figure, all simulations are included in the histogram on the left, while the histogram on the right includes only simulations in which failure occurs. Clearly, the volume of the sliding mass varies over a wide range. Figs. 6 and 7 show a simulation where a shallow failure occurs, while Figs. 8 and 9 show a simulation where a deep failure occurs. The consequences associated with these two failures are very different, which confirms the need to assess the consequence individually for each failure. In this study, the volume of the sliding mass is used to quantify the consequence, so that the risk is equivalent to the mean sliding mass of the failures.

Probabilistic parametric studies are also presented for the case where the horizontal and vertical spatial correlation lengths Θ_x and Θ_y are both varied in the range {0.25, 0.5, 1.0, 2.0, 4.0}. Figs. 10 and 11 show that increasing the horizontal spatial correlation

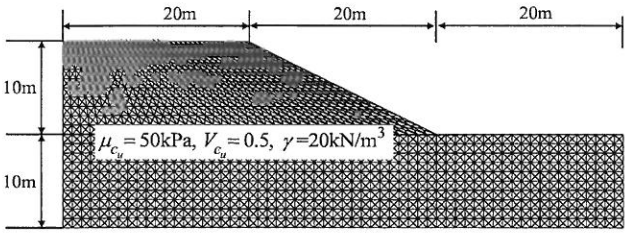

Fig. 4. Undrained slope in a uniform layer.

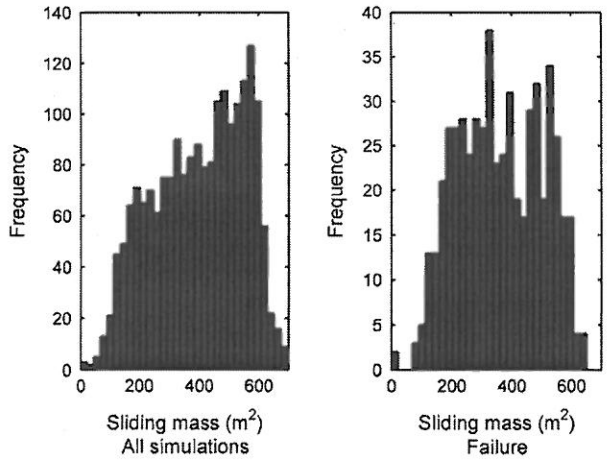

Fig. 5. Histogram of sliding mass ($\Theta_x = 2$, $\Theta_y = 0.25$, lower bound analysis).

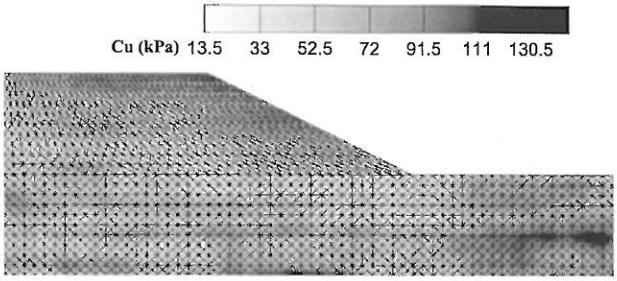

Fig. 6. A typical simulation of random field ($\Theta_x = 2$, $\Theta_y = 0.25$, shallow failure, dark and light regions depict "strong" and "weak" soils, respectively).

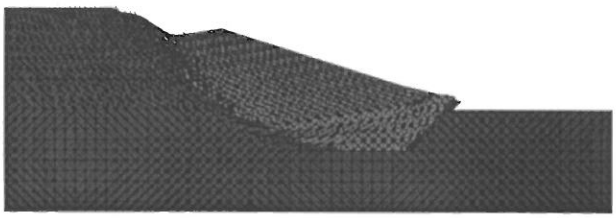

Fig. 7. A typical simulation by upper bound analysis ($\Theta_x = 2$, $\Theta_y = 0.25$, shallow failure, sliding mass is in red). (For interpretation of the references to colour in this figure legend, the reader is referred to the web version of this article.)

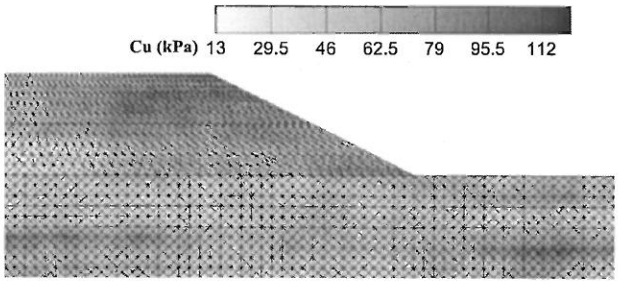

Fig. 8. A typical simulation of random field ($\Theta_x = 2$, $\Theta_y = 0.25$, deep failure, dark and light regions depict "strong" and "weak" soils, respectively).

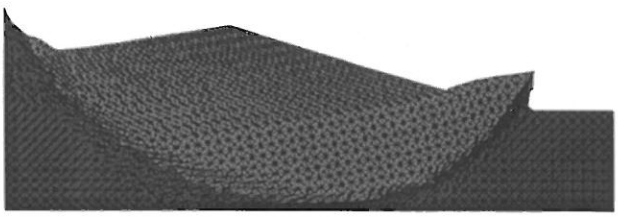

Fig. 9. A typical simulation by upper bound analysis ($\Theta_x = 2$, $\Theta_y = 0.25$, deep failure, sliding mass is in red). (For interpretation of the references to colour in this figure legend, the reader is referred to the web version of this article.)

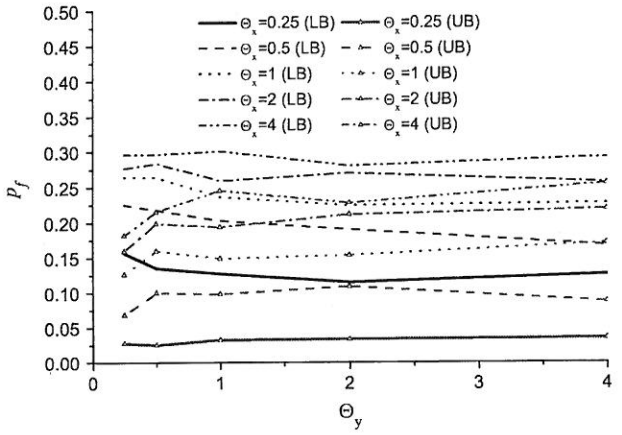

Fig. 10. Probability of failure by lower (LB) and upper (UB) bound analyses.

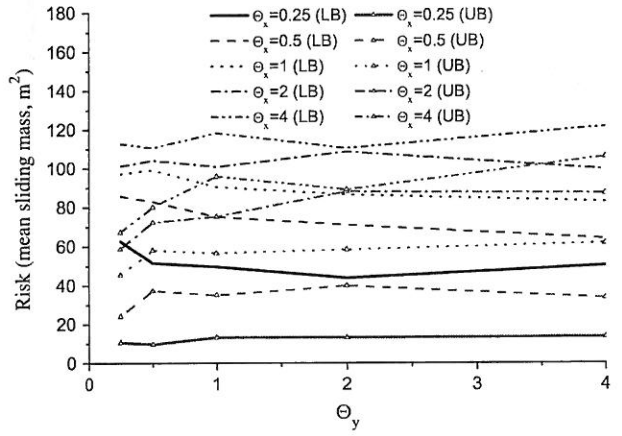

Fig. 11. Risk assessment by lower (LB) and upper (UB) bound analyses.

length will increase both p_f and the risk. The effect of the vertical spatial variability of the soil strength, however, is much less. Figs. 10 and 11 suggests a relatively large difference between the p_f obtained by lower and upper bound analyses. This is explained in Fig. 12, which shows that a small (less that 10%) difference in safety factor estimates would lead to a large (almost 10 times) difference in p_f. The relatively large differences between the lower and upper bound p_f estimates suggest that significant model uncertainties may exist, while lower bound analysis offers a conservative estimate.

5.2. Undrained failure in a two-layered slope

The profile of the slope in a two-layered soil deposit is shown in Fig. 13. The slope has a height $H = 24$ m, with the top layer having a unit weight of $\gamma_1 = 19$ kN/m^3 and an undrained shear strength $c_{u1} = 70$ kPa. The lower layer has the same unit weight but a higher shear strength of $c_{u2} = 100$ kPa. The boundary conditions are rollers on the left and right vertical boundaries, and full fixity at the base. Limit analyses showed that the lower and upper bounds of safety factor are 1.199 and 1.229, respectively. The safety factor obtained by an elasto-plasticity finite element analysis based on strength reduction method is 1.211.In the probabilistic analyses, the undrained shear strengths of the two layers are assumed to be log-normally distributed random variables with means $\mu_{c_{u1}} = 70$ kPa and $\mu_{c_{u2}} = 100$ kPa and coefficients of variation $V_{c_{u1}} = V_{c_{u2}} = 0.3$.

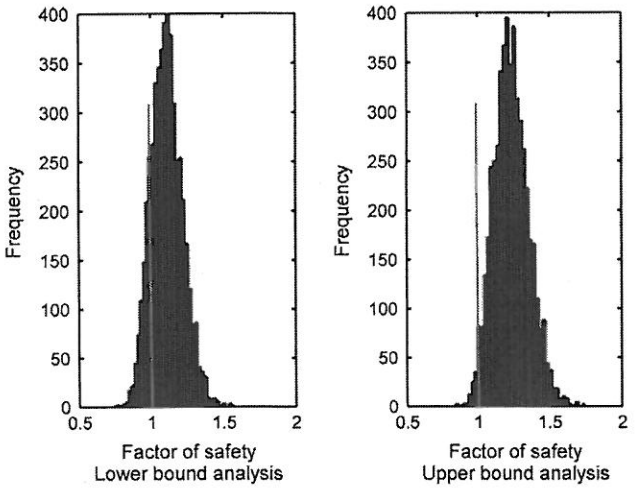

Fig. 12. Comparison of lower and upper bound analyses ($\Theta_x = 0.25$, $\Theta_y = 0.25$, p_f obtained by lower and upper bound analyses are 0.162 and 0.018, respectively).

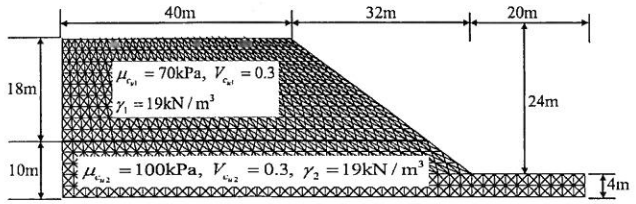

Fig. 13. A two layer slope.

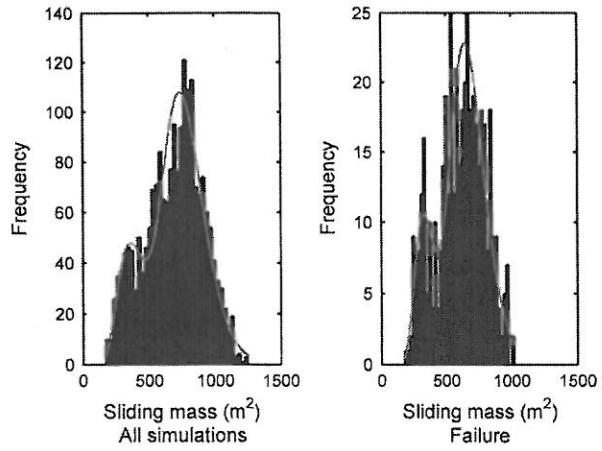

Fig. 14. Histograms of sliding mass ($\Theta_x = \Theta_y = 0.25$, lower bound analysis).

Two independent random fields are used to model the spatial variability of the shear strength, and only isotropic random fields are considered for the sake of simplicity.The histograms of the sliding mass under different spatial variability are shown in Figs. 14–19 for the lower bound analyses. These histograms illustrate clearly two (i.e., shallow and deep) failure mechanisms, which are more obvious when the spatial correlation lengths get larger. For the case of $\Theta_x = \Theta_y = 0.5$, Fig. 20 shows one typical shallow failure, while Fig. 21 shows one typical deep failure. It is interesting to note that in the second failure case, shallow and deep failures occur simultaneously (e.g., [7]).The two failure mechanisms can be separated by employing the Expectation Maximization (EM) algorithm (e.g., [1]). The distribution of the sliding mass is assumed to be a

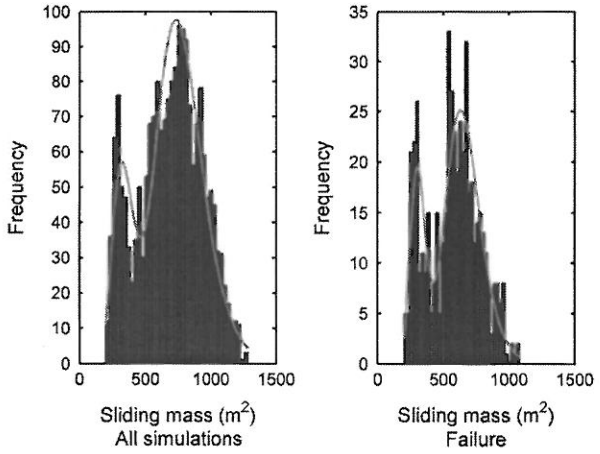

Fig. 15. Histograms of sliding mass ($\Theta_x = \Theta_y = 0.5$, lower bound analysis).

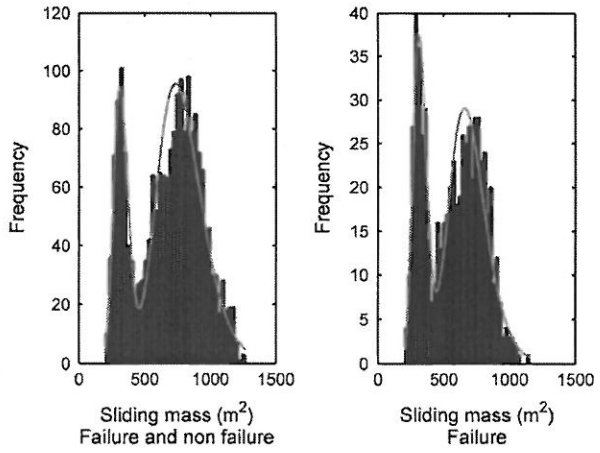

Fig. 16. Histograms of sliding mass ($\Theta_x = \Theta_y = 1$, lower bound analysis).

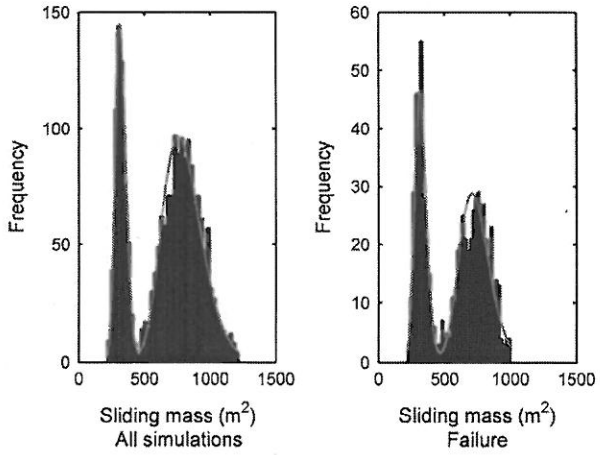

Fig. 17. Histograms of sliding mass ($\Theta_x = \Theta_y = 2$, lower bound analysis).

mixture of two lognormal distributions. The probability density function of the mixed model is

$$f_X(x) = \phi_s \frac{1}{x\sigma^s_{\ln X}\sqrt{2\pi}} \exp\left\{-\frac{1}{2}\left(\frac{\ln x - \mu^s_{\ln X}}{\sigma^s_{\ln X}}\right)^2\right\} + \phi_d \frac{1}{x\sigma^d_{\ln X}\sqrt{2\pi}} \exp\left\{-\frac{1}{2}\left(\frac{\ln x - \mu^d_{\ln X}}{\sigma^d_{\ln X}}\right)^2\right\} \phi_s + \phi_d = 1 \quad (18)$$

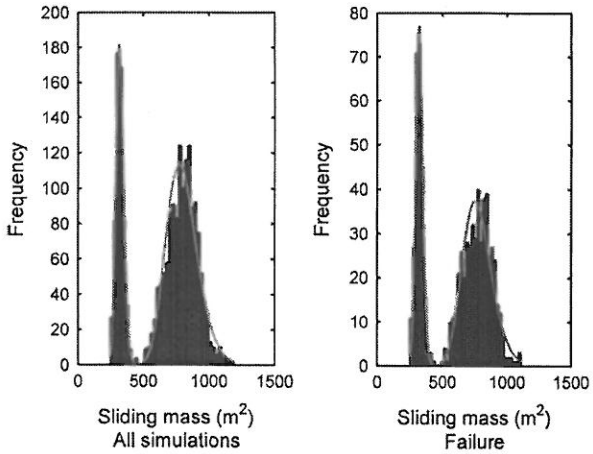

Fig. 18. Histograms of sliding mass ($\Theta_x = \Theta_y = 4$, lower bound analysis).

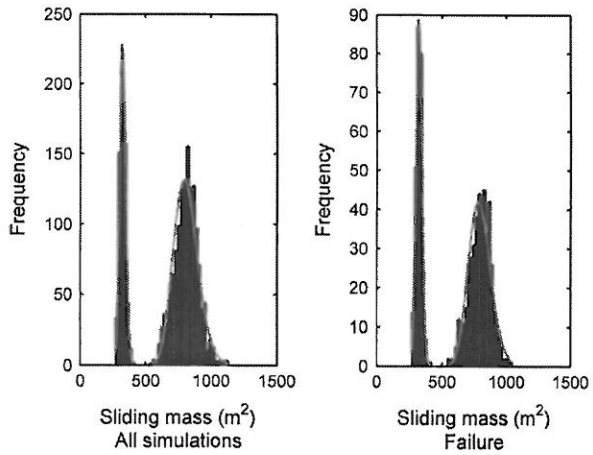

Fig. 19. Histograms of sliding mass ($\Theta_x = \Theta_y = 8$, lower bound analysis).

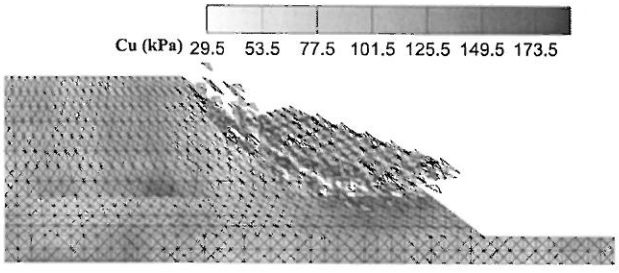

Fig. 20. A typical simulation by lower bound analysis ($\Theta_x = \Theta_y = 0.5$, shallow failure, dark and light regions depict "strong" and "weak" soils, respectively).

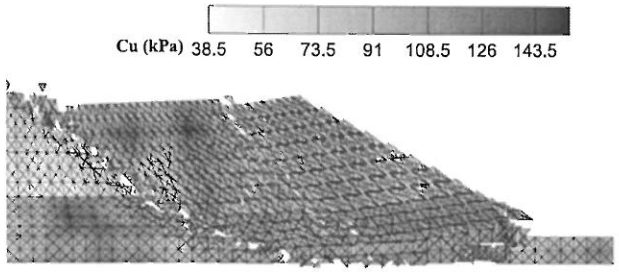

Fig. 21. A typical simulation by lower bound analysis ($\Theta_x = \Theta_y = 0.5$, deep failure, dark and light regions depict "strong" and "weak" soils, respectively).

Table 1
Mixture model of sliding mass (all simulations, lower bound analysis).

Θ	ϕ_d	μ_d (m^2)	σ_d (m^2)	ϕ_s	μ_s (m^2)	σ_s (m^2)
0.25	0.72	788.40	159.27	0.28	426.00	144.50
0.5	0.76	793.50	184.94	0.24	360.12	99.032
1.0	0.76	791.71	176.31	0.24	325.20	55.69
2.0	0.71	802.76	153.91	0.29	320.04	41.78
4.0	0.71	797.32	120.27	0.29	322.14	32.30
8.0	0.70	808.76	92.51	0.30	268.86	19.23

Table 2
Mixture model of sliding mass (failure only, lower bound analysis).

Θ	ϕ_d	μ_d (m^2)	σ_d (m^2)	ϕ_s	μ_s (m^2)	σ_s (m^2)
0.25	0.77	693.67	173.68	0.23	353.12	68.93
0.5	0.73	669.85	137.21	0.27	319.59	63.65
1.0	0.68	699.17	145.86	0.32	322.82	52.60
2.0	0.61	735.50	117.26	0.39	320.35	45.07
4.0	0.66	774.37	114.69	0.34	321.92	27.74
8.0	0.63	793.02	86.77	0.37	322.84	23.08

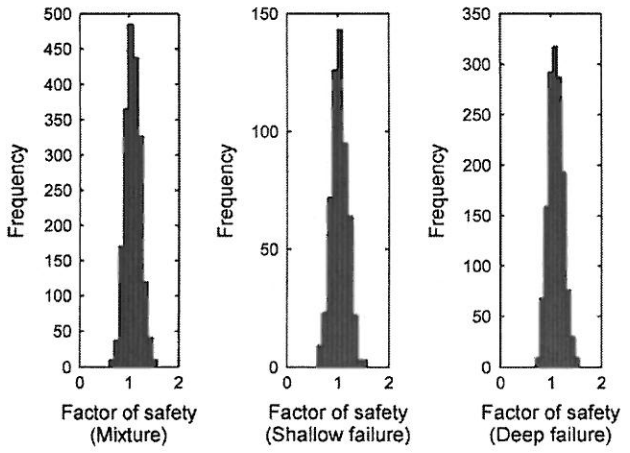

Fig. 22. Histograms of factor of safety ($\Theta_x = \Theta_y = 1$, lower bound analysis).

where ϕ_s and ϕ_d are the fractions of the shallow and deep failures, respectively.

Once the six parameters ϕ_s, ϕ_d, $\mu^s_{\ln X}$, $\sigma^s_{\ln X}$, $\mu^d_{\ln X}$ and $\sigma^d_{\ln X}$ in Eq. (18) have been calculated by the EM method, the means and standard deviations of the sliding mass corresponding to the shallow and deep failure mechanisms can be obtained. For example,

$$\mu_s = \exp(\mu^s_{\ln X} + \frac{1}{2}(\sigma^s_{\ln X})^2)$$
$$\sigma_s = \mu_s\sqrt{\exp\left((\sigma^s_{\ln X})^2\right) - 1} \tag{19}$$

where μ_s, and σ_s are the mean and standard deviation of the sliding mass of a shallow failure.

The fitted mixed model is plotted as the red[1] lines in Figs. 14–19. The mean and standard deviation of the volumes of the sliding mass are shown in Table 1 and Table 2. As mentioned previously, a complete assessment of the consequence of collapse should also quantify the dynamic behaviour of the sliding soil. As a preliminary estimate, the data in Table 2 can be used to estimate the risk. For example, one can estimate the risk as

[1] For interpretation of colour in Figs. 14–19, the reader is referred to the web version of this article.

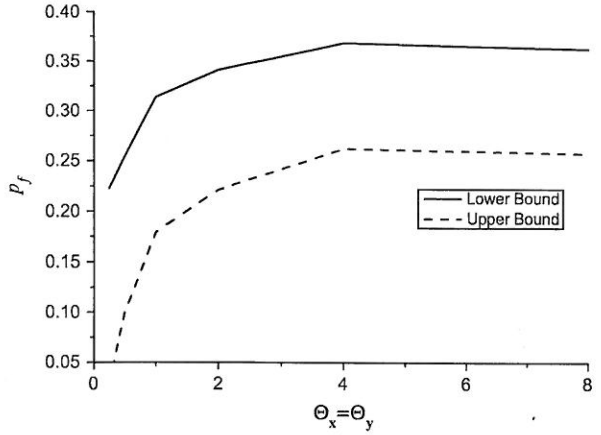

Fig. 23. Probability of failure by limit analysis.

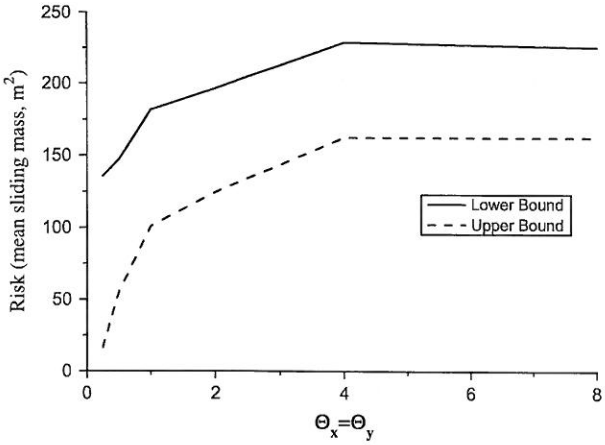

Fig. 24. Risk assessment by limit analysis.

$$R = p_f(\phi_s\mu_s C_s + \phi_d\mu_d C_d) \tag{20}$$

where C_s and C_d are the consequences of shallow and deep failures which can be assessed according to the mean sliding masses μ_s and μ_d.

The above estimate is more accurate than the one obtained from traditional methods (i.e., Eq. (1)) as it takes into account both shallow and deep failure mechanisms.

Since the failure mechanism of every simulation is identified, we can generate the histograms of the factor of safety of both failure mechanisms. Fig. 22 shows these plots for the lower bound analyses with $\Theta_x = \Theta_y = 1$. It can be seen that the distributions of the factor of safety for the two failure mechanisms are quite similar.

Figs. 23 and 24 show the influence of the spatial variability on p_f and risk, respectively. From these figures it can be seen that increasing the spatial correlation length increases both p_f and risk.

6. Concluding remarks

A new framework of quantitative risk assessment for landslides is proposed, which is based on the logic that the consequence should be assessed individually for each failure mode. Although only landslide risk is considered in this paper, the framework is generally applicable to other types of risk assessment in geotechnical engineering. For this study, consequence is assessed by computing the volume of the sliding mass. A more complete

assessment of consequence would model the dynamic behaviour of landslides, which is a future research objective.

Acknowledgements

The authors wish to acknowledge the support of the Australian Research Council in funding the Centre of Excellence for Geotechnical Science and Engineering. The first author would like to thank Dr. Zhiming Lu at Los Alamos National Laboratory and Dr. Xiang Ma at ExxonMobil Upstream Research Company for the helpful discussions on the Karhunen–Loeve expansion method.

References

[1] Bishop CM. Pattern recognition and machine learning. Springer; 2006.
[2] Cho SE. Effects of spatial variability of soil properties on slope stability. Eng Geol 2007;92(3–4):97–109.
[3] Chowdhury RN, Xu DW. Geotechnical system reliability of slopes. Reliab Eng Syst Saf 1995;47(3):141–51.
[4] Duncan JM. Factors of safety and reliability in geotechnical engineering. J Geotech Geoenviron Eng 2000;126(4):307–16.
[5] El-Ramly H, Morgenstern NR, Cruden DM. Probabilistic slope stability analysis for practice. Can Geotech J 2002;39(3):665–83.
[6] Fenton GA, Griffiths DV. Risk assessment in geotechnical engineering. Wiley; 2008.
[7] Griffiths DV, Lane PA. Slope stability analysis by finite elements, Geotechniqu 1999;49(3):387–403.
[8] Griffiths DV, Fenton GA. Influence of soil strength spatial variability on the stability of an undrained clay slope by finite elements. Slope stability 2000, Geotechnical special publications no. 101. ASCE; 2000. p. 184–93.
[9] Griffiths DV, Fenton GA. Probabilistic slope stability analysis by finite elements. J. Geotech Geoenviron Eng 2004;130(5):507–18.
[10] Griffiths DV, Huang JS, Fenton GA. Influence of spatial variability on slope reliability using 2-D random fields. J Geotech Geoenviron Eng 2009;135(10):1367–78.
[11] Huang JS, Griffiths DV, Fenton GA. System reliability of slopes by Rfem. Soils Found 2010;50(3):343–53.
[12] Huang SP, Quek ST, Phoon KK. Convergence study of the truncated Karhunen–Loeve expansion for simulation of stochastic processes. Int J Numer Meth Eng 2001;52(9):1029–43.
[13] Krabbenhoft K, Lyamin AV, Hjiaj M, Sloan SW. A new discontinuous upper bound limit analysis formulation. Int J Numer Meth Eng 2005;63(7):1069–88.
[14] Low BK, Gilbert RB, Wright SG. Slope reliability analysis using generalized method of slices. J Geotech Geoenviron Eng 1998;124(4):350–62.
[15] Lyamin AV, Sloan SW. Lower bound limit analysis using non-linear programming. Int J Numer Meth Eng 2002;55(5):573–611.
[16] Lyamin AV, Sloan SW. Upper bound limit analysis using linear finite elements and non-linear programming. Int J Numer Anal Meth Geomech 2002;26(2):181–216.
[17] Ma X, Zabaras N. A stabilized stochastic finite element second-order projection method for modeling natural convection in random porous media. J Comput Phys 2008;227(18):8448–71.
[18] Sloan SW. Lower bound limit analysis using finite-elements and linear-programming. Int J Numer Anal Meth Geomech 1988;12(1):61–77.
[19] Sloan SW. Upper bound limit analysis using finite-elements and linear-programming. Int J Numer Anal Meth Geomech 1989;13(3):263–82.
[20] Sloan SW, Kleeman PW. Upper bound limit analysis using discontinuous velocity-fields. Comput Methods Appl Mech Eng 1995;127(1–4):293–314.
[21] Zhang DX, Lu ZM. An efficient, high-order perturbation approach for flow in random porous media via Karhunen–Loeve and polynomial expansions. J Comput Phys 2004;194(2):773–94.
[22] Zhang J, Zhang LM, Tang WH. New methods for system reliability analysis of soil slopes. Can Geotech J 2011;48(7):1138–48.